

Platinum Group Metal-Doped Tungsten Phosphates for Selective C–H Activation of Lower Alkanes

Rhea Machado, Maria Dimitrakopoulou, Frank Girgsdies, Patricia Löser, Jingxiu Xie, Knut Wittich, Markus Weber, Michael Geske, Robert Glaum, Alexander Karbstein, Frank Rosowski, Sven Titlbach, Katarzyna Skorupska, Andrey V. Tarasov, Robert Schlögl, and Stephan A. Schunk*



Cite This: *ACS Catal.* 2022, 12, 13116–13130



Read Online

ACCESS |

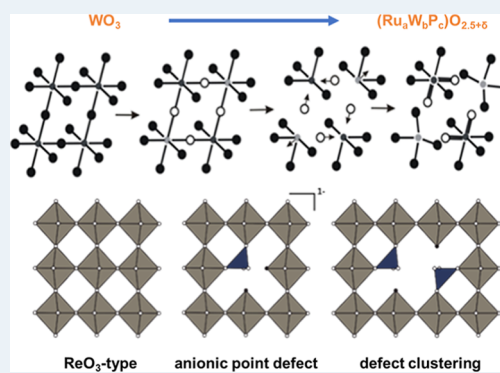
Metrics & More

Article Recommendations

Supporting Information

ABSTRACT: Platinum group metal (PGM)-based catalysts are known to be highly active in the total combustion of lower hydrocarbons. However, through an alternative catalyst design reported in this paper by isolating PGM-based active sites in a tungsten phosphate matrix, we present a class of catalysts for selective oxidation of *n*-butane, propane, and propylene that do not contain Mo or V as redox-active elements. Two different catalyst concepts have been pursued. Concept A: isolating Ru-based active sites in a tungsten phosphate matrix coming upon as ReO_3 -type structure. Concept B: dilution of PGM-based active sites through the synthesis of X-ray amorphous Ru tungsten phosphates supported on SiO_2 . Using a high-throughput screening approach, model catalysts over a wide compositional range were evaluated for C3 and C4 partial oxidation. Bulk crystalline and supported XRD amorphous phases with similar Ru/W/P compositions showed comparable performance. Hence, for these materials, composition is more crucial than the degree of crystallinity. Further studies for optimization on second-generation supported systems revealed even better results. High selectivity for *n*-butane oxidation to maleic anhydride and propane oxidation to an acrolein/acrylic acid has been achieved.

KEYWORDS: heterogeneous catalysis, C–H activation, selective oxidation, platinum group metals, ReO_3 -type structure, lower alkanes, *n*-butane oxidation, propane oxidation



INTRODUCTION

The utilization of small alkanes as a raw material for the chemical industry is an attractive option from both environmental and economic sustainability perspectives. Alkanes of interest are ethane, propane, and butane.¹ Small alkanes can be found in natural gas, which consists mainly of methane but also other lower alkanes. Other lower alkane feedstock sources are part of the streams within petrochemical or bio-refineries. In recent years, selective C–H activation of these molecules has received intense attention from both academia and industry.^{2,3} For instance, the oxidative dehydrogenation of lower alkanes to alkenes has been widely explored and debated.^{4,5} The selective oxidation of lower alkanes to oxygenates remains a challenging topic with large optimization potential. The reaction networks have a high degree of complexity, in which the C–C backbone must be preserved, C–H bonds must be activated, and C–O bonds have to be formed. Additionally, products usually show higher reactivity than alkanes, which may cause an over-oxidation of products.^{6–9} Regarding the oxyfunctionalization of alkanes, there is a general agreement in the scientific community that a suitable selective oxidation catalyst should follow certain principles. Grasselli proposed them in the form of seven pillars: importance of lattice oxygen, type of metal–

oxygen bond strength, host structure, redox behavior, multifunctionality of active sites, site isolation, and phase cooperation. Besides the abovementioned pillars, the nature of oxygen activation also has to be regarded.^{9–13}

Until now, the only industrial process for selective oxidation of lower alkanes to oxygenates is the production of maleic anhydride (MAN) from butane, with an annual world capacity of more than 1 million tons.¹⁴ With the industrial state-of-the-art catalyst, vanadyl pyrophosphate (VPP), a MAN yield of about 60% is achieved. Over the past 40 years, this catalyst has been improved by adding electronic promoters and optimizing the synthesis and activation procedures.^{15,16} Another prominent example, not realized in the industry, for selective oxidation of lower alkanes is the production of acrylic acid directly from propane. This reaction is catalyzed by MoVTenb

Received: May 31, 2022

Revised: September 21, 2022

mixed oxides in the form of an orthorhombic phase, M1.^{17–19} It is accepted today that the M1 structure is the active and selective phase, which is also known to catalyze the ammoxidation of propane to acrylonitrile and oxidative dehydrogenation of ethane to ethene.^{20,21} Other active phases which were reported as selective catalysts for alkane transformation are V–Sb mixed oxides useful in the ammoxidation of propane²² and Mo–V mixed oxides, which show appreciable selectivity in the oxidation of ethane to ethylene and acetic acid.²³ From the above said, it appears that V has been a critical element for the selective oxidation of lower alkanes.

Regarding the features of the host structure, a suitable structure should provide a framework of lattice oxygen that can accommodate the relevant cations in differing oxidation states and tolerate anion vacancies without causing structural collapse. Additionally, a fast electron transfer, vacancy, and lattice oxygen diffusion through the host structure are essential.¹⁰ Thereby, phosphates and tungsten oxides seem to be beneficial for the selective oxidation of *n*-butane to MAN. Cheng and Goddard^{24,25} conducted intensive density functional theory (DFT) calculations and proposed that phosphorus–oxygen bonds (P=O) are responsible for the activation of the C–H activation of butane. Recently, Roy et al.^{26,27} presented a new class of V^V/V^{IV}-containing mixed metal vanadium tungsten phosphates synthesized via solution combustion synthesis (SCS).^{28,29} This synthesis allowed the authors to precisely modify the V/W ratio of V_{1–x}W_xOPO₄, whereby two structures, depending on composition, have been crystallized: (0.04 ≤ *x* ≤ 0.26) led to α_{II}-VOPO₄ and (0 ≤ *x* ≤ 0.01) to β-VOPO₄. Schulz et al.³⁰ conducted catalytic studies using this new class of catalysts. They could show that the oxidation state of V in V_{1–x}W_xOPO₄, which can be tuned by tungsten content between 4.74 and 4.99, has a sensitive impact on MAN selectivity. Site isolation as a strategy for the selective activation of alkanes can be found in many publications and patents. In a BASF patent, V ions have been isolated in a tungsten phosphate matrix that is present as a ReO₃-type structure. Without containing VPP as a phase, performance studies of *n*-butane oxidation showed reasonable high selectivity toward MAN (*S* = 50% and *X* = 30%).³¹ Recently, Le et al. converted the unselective combustion catalyst Mn oxide into a catalyst for oxidative dehydrogenation of propane. Site isolation of the defect-rich MnO_x phase was achieved by using nanostructure and crystalline MnWO₄ as the support.³² However, selective catalysts without V for oxyfunctionalization of alkanes have not yet been identified.^{15,16}

While V- and Mo-based catalysts are often known to be selective for partial oxidation reactions, catalysts based on platinum group metal (PGM) in their metallic form are traditionally known as efficient total combustion catalysts for small hydrocarbons.^{33,34} This high oxidation potential could turn into a positive feature if the right oxide matrix for the PGM can be identified, which allows keeping the metal in oxidized form; it could be expected that due to the high oxidizing ability of PGMs, milder conditions such as lower reaction temperatures could be used, thereby preventing overoxidation of highly reactive intermediates and consecutive oxidation of the desired products. Furthermore, such a matrix could add additional beneficial functionalities: using density functional theory (DFT) calculations, the ability of highly reactive phosphorus–oxygen double bonds (P=O) to activate C–H bonds of butane was recently proposed by Cheng and Goddard.^{24,25} Wang et al. further showed that this

process could be viewed as a proton-coupled electron transfer.³⁵ Zhang et al. used reflection absorption infrared spectroscopy and DFT calculations to establish the active site for selective C–H activation of propane to be Pd²⁺ of PdO(101). They could show strong evidence for the formation of propane σ-complexes on the PdO(101) surfaces, which seem to be crucial for the selective C–H cleavage.³⁶ Martin et al. published a recent review about alkane activation on late-transition-metal oxides determined mainly from ultrahigh-vacuum surface science and DFT calculations. They highlighted the above-discussed importance of adsorbed alkane σ-complexes and reviewed that there are strong indications that this adsorption behavior also occurs on RuO₂(110) and IrO₂(110) surfaces.³⁷ Ruthenium is highly active in selectively catalyzing the conversion of a wide range of organic compounds to carbon dioxide. In the field of wet air oxidation, ruthenium is one of the most promising noble metals for the reduction of pollutants. Barbier et al. studied the degradation of phenol over Ru, Pd, and Pt supported on CeO₂. It was found that Ru showed the highest stability and activity in phenol oxidation.^{38,39} In recent years, various groups were involved in efforts demonstrating that homogeneous PGM-based catalysts and single-atom PGM-based have potential in selective C–H activation of alkanes. Nevertheless, only a few reports on the formation of oxygenates over PGM-based catalysts can be found. Most notably, Periana et al. showcased Pt-based homogeneous catalysts, stabilized in sulfuric acid, to be highly efficient in terms of yield in C–H activation of methane.⁴⁰ Palkovits et al. followed upon the work of Periana et al. to develop Pt-based heterogeneous catalysts in sulfuric acid for selective methane oxidation in the presence of SO₃, which can be recovered as sulfate ester.⁴¹ Besides Pt, single-atom Rh-based supported heterogeneous catalysts were also highlighted to activate the C–H bond of methane selectively.^{42–44} In addition to Pt and Rh, single Pd atoms homogeneously distributed in Ga liquid phase and supported on porous glass were recently reported by Taccadi et al. to catalyze butane dehydrogenation.⁴⁵ Subnanometer Pt clusters were also concluded by Vajda et al. to catalyze oxidative dehydrogenation of propane.⁴⁶ While SbO_x itself is only able to convert isobutylene to methacrolein, Inoue et al. could show that Pt on SbO_x catalysts was active for isobutane oxidation to methacrolein with a reasonable high selectivity of 57%. They suggested that dehydrogenation of isobutane to isobutylene occurs on the Pt–SbO_y site in the presence of oxygen, and the Sb₆O₁₃ phase catalyzes the consecutive selective oxidation of isobutylene to methacrolein. Although their catalyst exhibits a remarkable methacrolein selectivity, it must be mentioned that the overall yield never exceeds 0.5%. Hence, these catalysts are at present not a serious (industrially viable) alternative to catalysts consisting of vanadium.^{47,48}

Nonetheless, in the last 2 decades, much scientific work has been carried out to show that ruthenium catalysts can activate alkanes. Ru is generally accepted as one of the best catalysts for partial oxidation of methane to syngas.^{49–51} Balkus et al. designed a zeolite-encapsulated ruthenium catalyst for oxidation of cyclohexane to the cyclic ketone, which showed 10 times higher activity (*X* = 70%) than its homogeneous alternative. They proposed that such high conversions are only possible due to site isolation of the active species.⁵² The strategy of active site isolation for PGM catalysts seems to enhance selectivity and leads to promising candidates for selective oxidations.

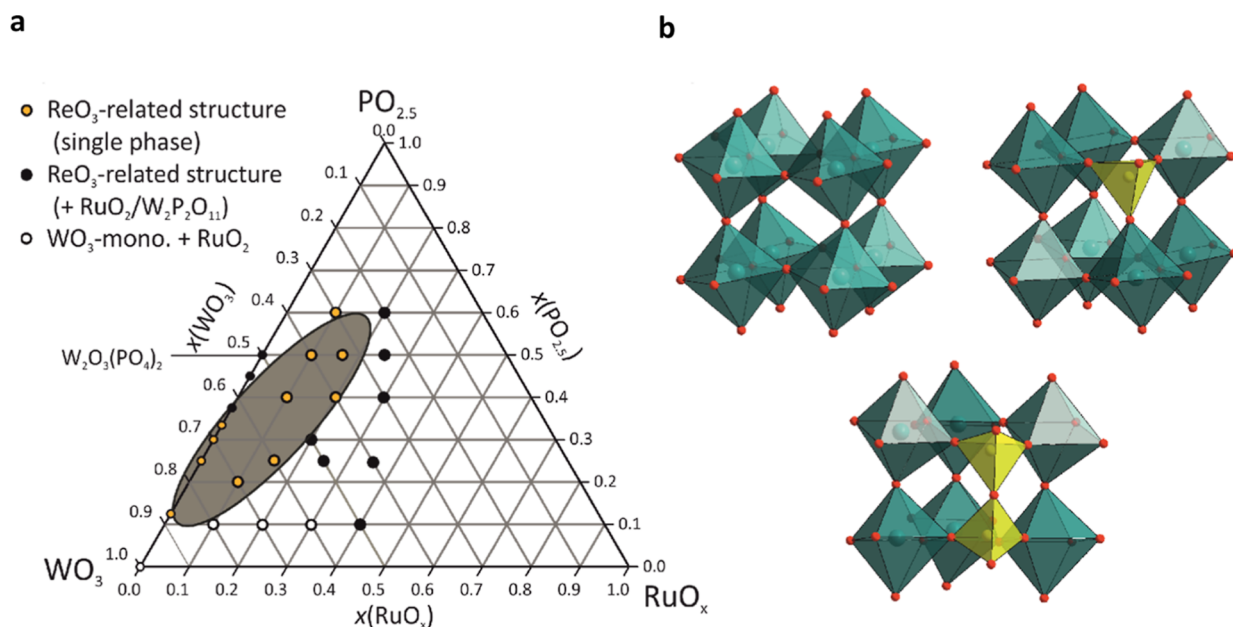


Figure 1. (a) Compositional diagram for the ternary system $\text{WO}_3/\text{RuO}_x/\text{PO}_{2.5}$ showing the region (gray ellipse) of single-phase formation of unsupported catalyst material ($\text{Ru}_a\text{W}_b\text{P}_c\text{O}_{2.5+\delta}$) with ReO_3 -related crystal structure. (b) ReO_3 -type structure with substitution of octahedra $[\text{MO}_6]$ by one and two phosphate tetrahedra, respectively.

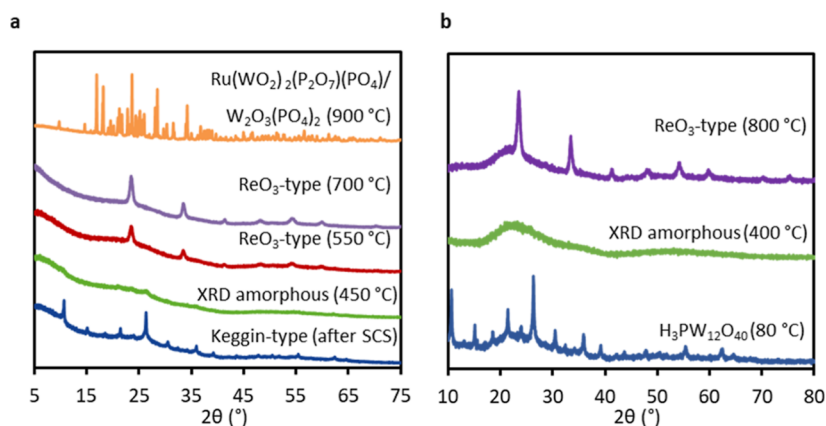


Figure 2. XRPD pattern of fresh Ru tungsten phosphates. (a) Unsupported $(\text{Ru}_{0.1}\text{W}_{0.4}\text{P}_{0.5})\text{O}_{2.5+\delta}$ at different calcination temperatures. (b) Supported ruthenium tungsten phosphates containing $\text{Ru}/\text{W}/\text{P} = 0.05:0.35:0.6$ at different calcination temperatures.

In this work, we present a new synthetic approach to vanadium-free heterogeneous catalysts for selective oxidation of lower alkanes to oxygenates. Accordingly, one dogma for selective oxidation of lower alkanes was broken; namely, vanadium is an essential component in the production of oxygenates from lower alkanes. Our approach isolates Ru-based active sites in non-zero valent form for transforming PGMs into selective oxidation catalysts. In order to realize a high dispersion of Ru species, we have adopted two different catalyst concepts. Concept A: unsupported crystalline tungsten phosphates containing Ru (or Rh or Pd) by changing calcination temperature, we could obtain XRD-amorphous catalysts.⁵³ These form solids with ReO_3 -related XRPD patterns when treated at higher temperatures. In Figure 1a, the ternary compositional diagram of $\text{WO}_3\text{--RuO}_x\text{--PO}_{2.5}$ is displayed. Compositions can be represented by the general formula $(\text{Ru}_a\text{W}_b\text{P}_c)\text{O}_{2.5+\delta}$. Only compositions with $0 < a < 0.25$, $0.25 < b < 0.9$, and $0.01 < c < 0.5$ lead to a ReO_3 -related structure for the unsupported catalyst (see Figure 1b). In our

catalyst Concept B, amorphous phase analogues consisting of Ru and W dispersed in poly-phosphoric acid networks supported on silica are employed. This approach enables the synthesis of catalysts over the whole ternary composition range, and additionally, the specific inclusion of promoters is possible. Both classes of catalysts were studied for butane oxidation. The supported catalysts were also studied for propane and propylene.

RESULTS

Catalysts. Unsupported ruthenium tungsten phosphates were synthesized by solution combustion synthesis (SCS) and subsequent calcination and are listed in Supporting Information Table S1 (Concept A). An exhaustive structure study of ReO_3 -type tungsten phosphates containing PGMs can be found in ref⁵⁴. Figure 2a shows the XRD pattern of all $(\text{Ru}_{0.1}\text{W}_{0.4}\text{P}_{0.5})\text{O}_{2.5+\delta}$ samples calcined at low (450 °C), middle (550–700 °C), and high (900 °C) temperatures. The solid material without further calcination showed only reflections of

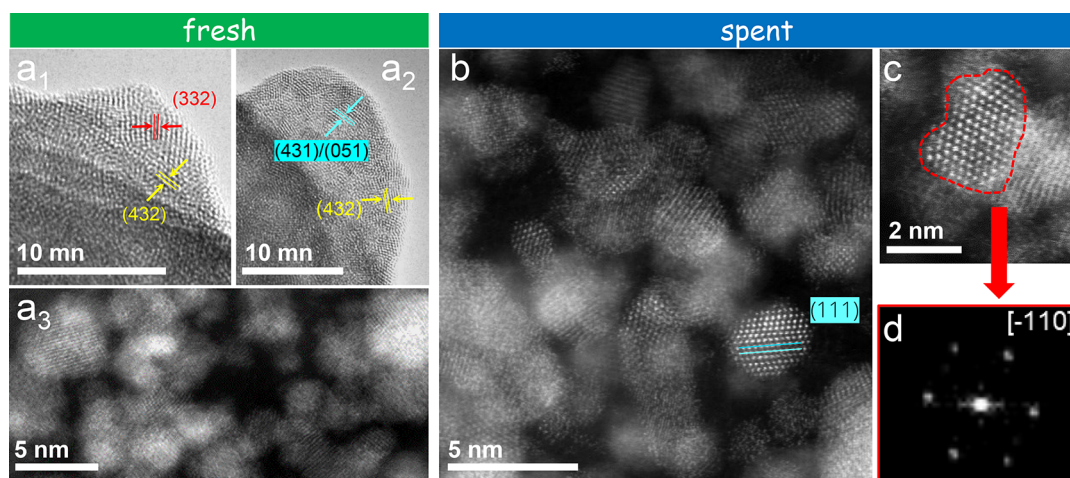


Figure 3. Electron microscopic structural analysis of fresh and spent unsupported $(\text{Ru}_{0.1}\text{W}_{0.4}\text{P}_{0.5})\text{O}_{2.5+\delta}$ calcined at 450 °C. Fresh catalyst: (a₁,a₂) HRTEM images of the sample showing crystalline nanofeatures with Keggin-type structure as indicated by the lattice planes. (a₃) High-resolution HAADF-STEM image of an overview of the sample showing the formation of nanoparticles with size, mainly smaller than 5 nm. Spent catalyst: (b) HR-STEM showing highly oriented nanoparticles. The detection of (111) lattice planes of $(\text{Ru}_{0.1}\text{W}_{0.4}\text{P}_{0.5})\text{O}_{2.5+\delta}$ with ReO_3 -type structure is highlighted in light blue color. (c,d) HR-STEM image of a single nanoparticle oriented along the $[\bar{1}10]$ zone axis marked with a red dashed line and its corresponding FFT pattern ($(\text{Ru}_{0.1}\text{W}_{0.4}\text{P}_{0.5})\text{O}_{2.5+\delta}$ with ReO_3 -type structure), respectively.

Keggin-related structures with a significant contribution of XRD-amorphous background. This is due to the incomplete combustion of the precursors after synthesis, which was verified by the elemental analysis (Supporting Information Table S2), and likely because of a nanocrystalline morphology. After calcination in air at 450 °C for 1 day, the solid material $((\text{Ru}_{0.1}\text{W}_{0.4}\text{P}_{0.5})\text{O}_{2.5+\delta}$ calc. at 450 °C) became XRD amorphous. TG–MS analysis revealed a significant amount of carbon-related species. The mass loss profile is accompanied by an evolution of CO_2 as can be seen on the mass spectra (Supporting Information Figure S1a,b). The formation of CO_2 lasts over the whole temperature range and prevails at temperatures above 700 °C. These very resistant carbon-related species originate from the incomplete combustion of glycine, used as fuel in the SCS. They may appear in the form of carbonaceous deposits and dissolved carbon. No evidence for the presence of carbidic species was obtained by XRD analysis or in transmission electron microscopy (TEM) examination. Upon intermediate calcination temperatures in air at 550 °C for 3 days or 700 °C for 2 days, the homogeneous, thermodynamically metastable solid materials showed the characteristic crystalline ReO_3 -related structure (see Figure 2a). A Rietveld refinement using tetragonal WO_3 as a structure model yielded an average volume-weighted domain size in the range of 15–20 nm. A further increase in calcination temperature to 900 °C led to equilibration with the formation of phase mixtures consisting of $\text{Ru}(\text{WO}_2)_2(\text{P}_2\text{O}_7)$ (PO_4) and monoclinic $\text{W}_2\text{O}_3(\text{PO}_4)_2$. The bulk crystal structure of the catalysts with ReO_3 -related structure was preserved during catalysis (see Supporting Information Figure S2). The catalyst without calcination lost its Keggin-type structure and became XRD amorphous. The sample consisting of $\text{Ru}(\text{WO}_2)_2(\text{P}_2\text{O}_7)$ -(PO_4) and monoclinic $\text{W}_2\text{O}_3(\text{PO}_4)_2$ was still containing the phases after catalysis, with one unidentified reflection showing higher intensity (see Supporting Information Figure S3). The low-temperature CO_2 evolution segment at 450 °C (see Supporting Information Figure S1a) almost vanished, and the high-temperature peak was significantly reduced after the catalytic studies, indicating partial liberation out of carbona-

ceous formations during catalytic operation. Despite the significant carbon content, the ICP-OES analysis confirmed the consistency of the composition for the selected spent (catalysts after catalysis) and fresh samples for Ru, W, and P (see Supporting Information Tables S2 and S3). Due to the synthesis protocol and high calcination temperatures, the BET surface areas of fresh catalyst were between 1 and 15 m^2/g . However, the BET surface areas after catalytic studies ranged between 2 and 8 m^2/g (see Supporting Information Tables S2 and S3). The total carbon content decreases with higher annealing temperature, which was verified by the elemental analysis. The synthesis of these Ru/W/P/O phases led to a relatively high carbon content (see Supporting Information Tables S2 and S3 and Supporting Information Figure S1b).

Supported Ru tungsten phosphates (Concept B) with varied Ru/W/P, Ru/W/P/Te, or Ru/W/P/Te/M (M: Sb or Ta) compositions were synthesized with incipient wetness impregnation of corresponding precursors on SiO_2 (see Supporting Information Table S4). The BET surface area of the fresh material was 77 m^2/g and decreased marginally after catalysis to 72 m^2/g . Figure 2b shows XRD patterns of supported PGM tungsten phosphates containing Ru/W/P = 0.05:0.35:0.6 treated at different temperatures. After drying at 80 °C, the catalysts exhibited the reflections assigned to dodecatungstophosphoric acid. After calcination at 400 °C, the catalyst became XRD amorphous. Remarkably, at a calcination temperature of 800 °C, the catalyst showed the characteristic crystalline ReO_3 -related structure, as already observed for unsupported catalysts, calcined at temperatures between 550 and 700 °C (see Figure 2a). In Supporting Information Figure S4, representative XRD patterns of this class of materials with different elemental compositions are displayed. After drying at 80 °C, the catalysts were either XRD-amorphous or exhibited reflection of telluric acid. According to XRD analysis, SiO_2 -supported catalysts were XRD amorphous after catalysis (see Supporting Information Figure S5).

HRTEM and high-angle annular dark-field scanning transmission electron microscopy (HAADF-STEM) investigations of unsupported ruthenium tungsten phosphate with a

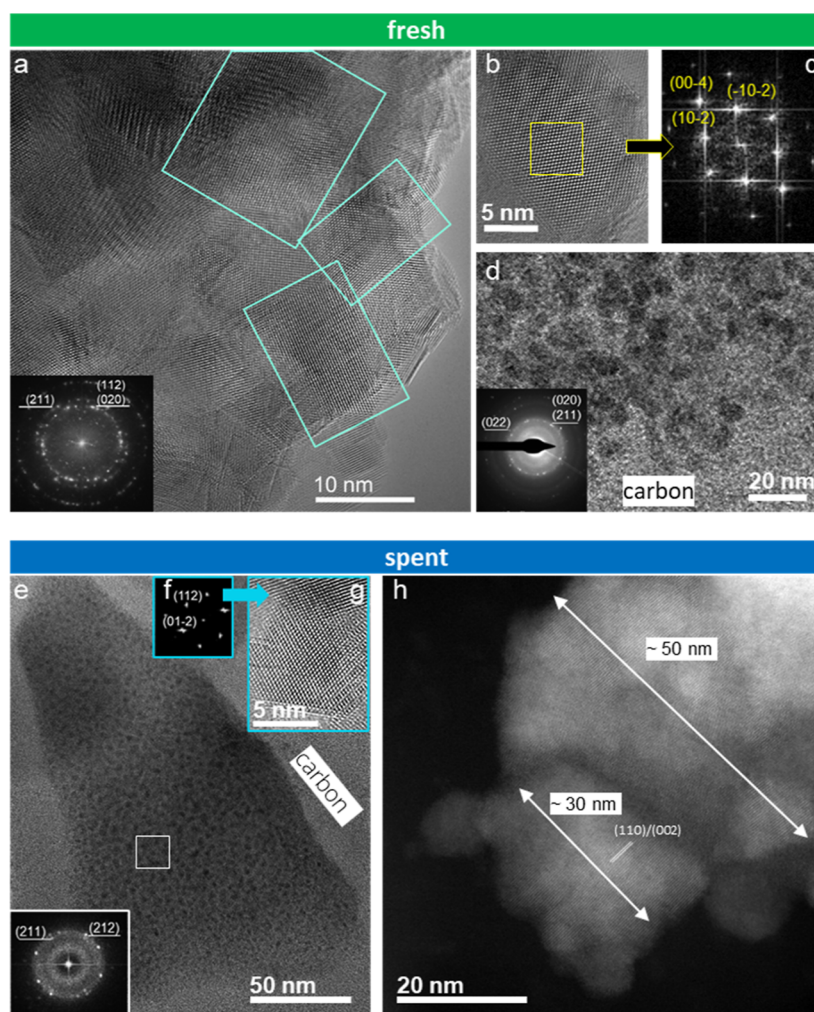


Figure 4. Electron microscopic structural analysis of fresh and spent unsupported $(\text{Ru}_{0.1}\text{W}_{0.4}\text{P}_{0.5})\text{O}_{2.5+\delta}$ calcined at 700 °C. Fresh catalyst: (a) HRTEM image of the sample consisted of various crystals with a diameter larger than 10 nm (inset: FFT pattern). (b) HRTEM image of a single crystal and (c) its corresponding FFT pattern. (d) HRTEM image of the sample revealing the formation of particles with a diameter less than 10 nm and SAED pattern (inset). Spent catalyst: (a) HRTEM image of an overview of the sample showing the formation of crystal nanoparticles with a diameter smaller than 10 nm (inset: FFT from the white selected area). (g) HRTEM image of a single nanocrystal with its corresponding FFT in the inset. (f) HAADF-STEM image of the sample also illustrating the formation of larger crystals (>10 nm). In both systems, the polycrystalline nature of the sample and the tetragonal phase of WO_3 were confirmed through the occurrence of ring diffraction patterns and their indexing.

composition of $(\text{Ru}_{0.1}\text{W}_{0.4}\text{P}_{0.5})\text{O}_{2.5+\delta}$ calcined at low-temperature (450 °C) and moderate-temperature range (700 °C) were conducted. While $(\text{Ru}_{0.1}\text{W}_{0.4}\text{P}_{0.5})\text{O}_{2.5+\delta}$ calcined at 450 °C is clearly XRD amorphous, the HRTEM and high-resolution HAADF-STEM images in Figure 3a₁–a₃ show the highly polycrystalline quality of this material and nanostructures with an average particle size ranging from sub-nanometer up to about 5 nm in diameter. The ReO_3 -type (700 °C) catalyst revealed a polycrystalline structure with an inhomogeneous morphology. It consists of different-sized spherical and non-spherical nanoparticles ranging from nanometer to larger than 10 nm, as shown in Figure 4a,d.

Further microscopic studies of the spent catalyst calcined at the middle-temperature range confirmed that the morphology and crystallinity are fully preserved. In more detail, the catalyst includes polycrystalline nanostructures with the same size range as the fresh catalyst based on the high-resolution HAADF-STEM image shown in Figure 3b. Also, the spent catalyst calcined at a moderate temperature range (700 °C) with the ReO_3 -type structure exhibited a similar morphology to

the fresh one. The system consists of many nanocrystals of varying shape, size, and growth orientations. In Figure 4e, an HRTEM image taken from a sample region consisting of nanoparticles with an average size smaller than 10 nm is depicted. TEM data for the fresh and spent sample are entirely consistent with the XRD studies, and for calcination temperatures up to 700 °C, no phase formation of RuO_2 was detected. Likely, the numerous nanoparticles with less than 10 nm diameter found in both samples give rise to the broad profiles of the corresponding X-ray diffractograms (Figure 2a). EDS elemental mapping analysis of the fresh and spent catalysts for both calcination temperatures 450 and 700 °C provided evidence for homogeneous distribution of the elements W, P, Ru, and O (Supporting Information Figures S6 and S7). Local and overall elemental characterization of the spent catalyst showed that the system exhibits the same quantitative chemical composition as that of the fresh catalyst.

In Figure 5, HRTEM investigations of fresh and spent supported ruthenium tungsten phosphates containing Ru/W/P = 0.05:0.35:0.6 are represented. The HRTEM image of the

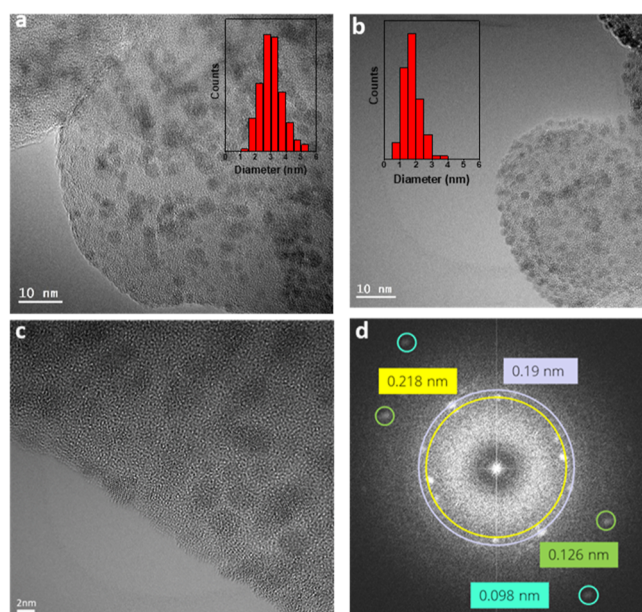


Figure 5. Electron microscopic structural analysis of fresh and spent supported ruthenium tungsten phosphate with a compositional ratio Ru/W/P = 0.05:0.35:0.6. Fresh catalyst: (a) HRTEM image of the sample consisted of various crystals with a diameter smaller than 6 nm and the related particle size histogram spent catalyst, (b) HRTEM image of an overview of the sample showing the formation of crystal nanoparticles with a diameter smaller than 4 nm and the related particle size histogram, and (c) HRTEM image and its corresponding FFT pattern (d). In total, 200 particles were measured for each particle size histogram and the bin size was 0.5.

fresh catalyst (Figure 5a) revealed nanoparticles with an average size smaller than 5 nm. After catalysis, the supported catalyst exhibited nanoparticles with an average size smaller than 3 nm, which can be perceived in Figure 5b. This observation fully agrees with XRD studies, which showed the spent catalyst to be XRD amorphous (see the Supporting Information Figure S5). The FFT pattern (Figure 5d) taken from a selected area (Figure 5c) does not allow for distinguishing between $c\text{-H}_3(\text{PW}_{12}\text{O}_{40})(\text{H}_2\text{O})_3$ (HPA), $c\text{-WO}_3$, or $t\text{-WO}_3$ structures for the ruthenium-containing catalyst material (see Supporting Information Table S6). However, Rietveld refinements of nearly amorphous unsupported material (450 °C calcination temperature) with a combination of $t\text{-WO}_3$ (for the ruthenium containing phase) and cubic HPA (particle size < 1 nm) showed that the material had more structural similarities to $t\text{-WO}_3$ than to HPA (see Supporting Information Figure S8). Considering that the XRD of supported and unsupported materials look similar, the nanoparticles of the supported catalyst have a $t\text{-WO}_3$ structure. Further corroboration is provided by XRD studies of the corresponding catalyst calcined at 800 °C (see Figure 2b), which exhibits, exclusively, reflections of a ReO_3 -related crystalline phase. It seems that at higher calcination temperatures, the nanoparticles agglomerated to larger particles, which enabled the visibility of crystallinity by XRD studies. EDS elemental mapping analysis of the fresh and spent supported catalysts demonstrated a homogeneous distribution of the elements W, P, Ru, and O but also contamination of C (see Supporting Information Figure S9).

XPS measurements have been carried out on representative samples before and after catalytic testing. For a detailed

description of the analysis procedure and deconvolution of the spectra please and an overview of the method used for fitting, please see the Supporting Information regarding methods. The results have to be seen in the light that no detailed reference spectra are available for this class of tungsten–phosphate-based compounds. From the XPS measurements, it can be concluded that ruthenium is present in the valence states of +III and +IV. Table 1 shows the ratios of Ru(+III) to Ru(+IV) for a selected

Table 1. XPS Analysis of Unsupported Ruthenium Tungsten Phosphates (Concept A) vs Supported Ruthenium Tungsten Phosphates (Concept B)

unsupported		Ru III	Ru IV	Ru III/IV	
(Ru _{0.1} W _{0.4} P _{0.5})O _{2.5+δ}	700 °C calcined	fresh	69	31	2.22
(Ru _{0.1} W _{0.4} P _{0.5})O _{2.5+δ}	700 °C calcined	spent	68	32	2.12
(Ru _{0.1} W _{0.4} P _{0.5})O _{2.5+δ}	550 °C calcined	fresh	65	35	1.86
(Ru _{0.1} W _{0.4} P _{0.5})O _{2.5+δ}	550 °C calcined	spent	67	33	2.03
(Ru _{0.1} W _{0.4} P _{0.5})O _{2.5+δ}	450 °C calcined	fresh	82	18	4.55
(Ru _{0.1} W _{0.4} P _{0.5})O _{2.5+δ}	450 °C calcined	spent	72	28	2.57
supported		Ru III	Ru IV	Ru III/IV	
0.5Ru/0.35W/0.6P	fresh	31	59	0.52	
0.5Ru/0.35W/0.6P	spent	16	84	0.19	
0.5Ru/0.45W/0.5P	fresh	45	55	0.82	
0.5Ru/0.45W/0.5P	spent	22	78	0.28	

number of fresh and spent samples (see Supporting Information Table S9 and Supporting Information Figures S10 and S11). In contrast to the presence of ruthenium in two valence states for tungsten, the main species corresponding to the valance state of +VI could be detected; pentavalent tungsten species represent a minority amount. We take the result as indicative that ruthenium that is present in more than one oxidation state in the catalytic materials may therefore represent the catalytic redox element. Supported and unsupported samples do show pronounced differences in the ratio of Ru(+III) to Ru(+IV), which may explain some of the differences in the performance of these materials. Within the scope of this work, we want to discuss these results only as indicative, further investigations, especially investigations under reaction conditions, will have to be done in the future to elucidate additional details.

C–H Activation of Butane: Catalytic Behavior of Unsupported Crystalline Ru Tungsten Phosphates. The catalytic performance was evaluated at $350 \leq T \leq 450$ °C, $p = 1$ bar, $\text{C}_4\text{H}_{10}/\text{O}_2/\text{H}_2\text{O} = 2:20:3\%$ vol, and $\text{GHSV} = 2000 \text{ h}^{-1}$, and the main findings for the unsupported Ru tungsten phosphates are illustrated in Figure 6. For reference, $(\text{W}_{0.75}\text{P}_{0.25})\text{O}_{2.5+\delta}$ was catalytically inactive under these reaction conditions (see Figure 6a). The catalytic activity at different reaction temperatures is shown in Figure 6a,b. $(\text{Ru}_{0.1}\text{W}_{0.4}\text{P}_{0.5})\text{O}_{2.5+\delta}$ samples calcined at low (450 °C) and middle (550–700 °C) temperature ranges exhibited similar activity for the range of reaction temperatures, while $(\text{Ru}_{0.1}\text{W}_{0.4}\text{P}_{0.5})\text{O}_{2.5+\delta}$ without calcination or calcined at high-temperature range (900 °C) were less active. From Figure 6c, the corresponding MAN yield as a function of reaction temperatures is depicted. For all catalysts, around 25% MAN selectivity was obtained (see Figure 6d). However, due to the higher activity of catalysts calcined at 450–700 °C, yields of those are higher than those with a Keggin-type structure (after SCS) and with a $\text{Ru}(\text{WO}_2)_2(\text{P}_2\text{O}_7)(\text{PO}_4)/\text{W}_2\text{O}_3(\text{PO}_4)_2$ phase mixture (900 °C). This trend did not change even if BET

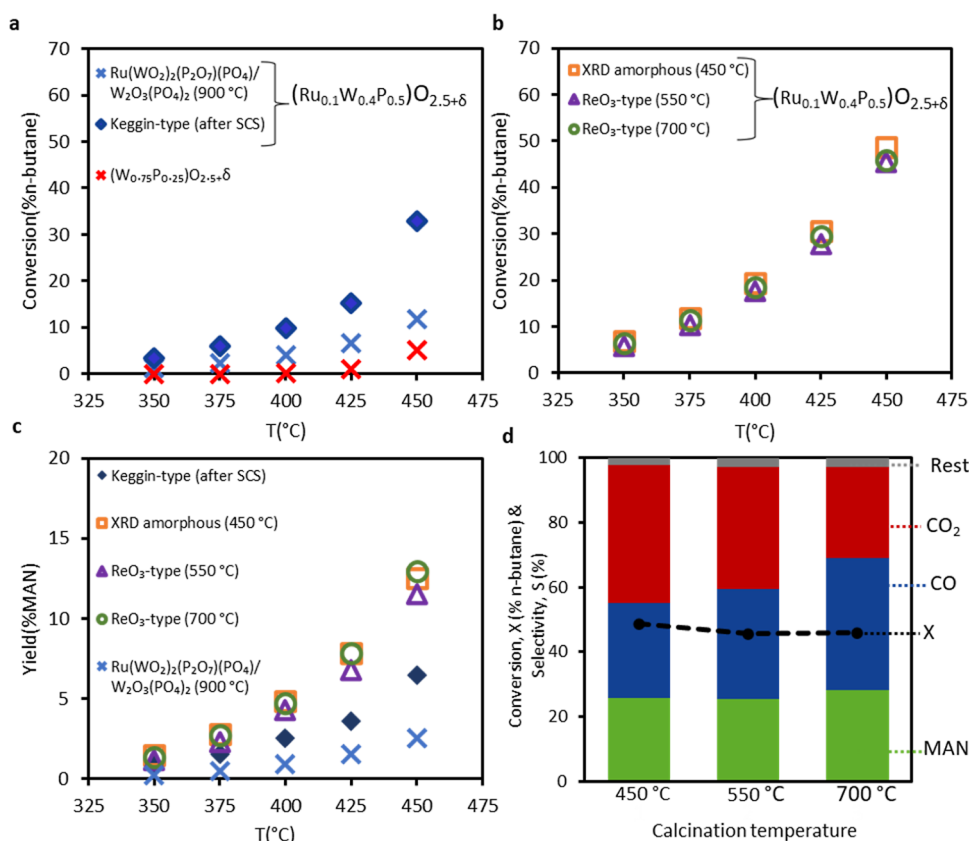


Figure 6. Catalytic performance of unsupported ruthenium tungsten phosphates for selective oxidation of butane. (a) Conversion of $(W_{0.75}P_{0.25})O_{2.5+\delta}$ and $(Ru_{0.1}W_{0.4}P_{0.5})O_{2.5+\delta}$ directly after SCS (Keggin type) and calcined at 900 °C, as a function of temperature. (b) Conversion of $(Ru_{0.1}W_{0.4}P_{0.5})O_{2.5+\delta}$ calcined at low (450 °C) and middle (550–700 °C) temperature range, as a function of temperature. (c) MAN yield of $(Ru_{0.1}W_{0.4}P_{0.5})O_{2.5+\delta}$ calcined at different temperatures as a function of temperature. (d) Conversion and product selectivity of major products of $(Ru_{0.1}W_{0.4}P_{0.5})O_{2.5+\delta}$ calcined at low (450 °C) and middle (550–700 °C) temperature ranges. Rest = summation of all detected products, excluding CO, CO₂, and MAN. Reaction conditions: 450 °C, 1 bar, C₄H₁₀/O₂/H₂O = 2:20:3, and 2000 h⁻¹.

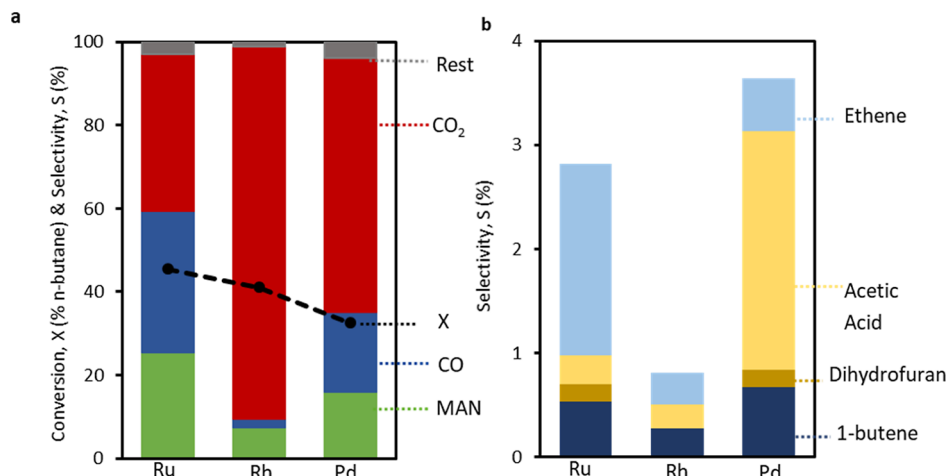


Figure 7. Catalytic performance of unsupported PGM tungsten phosphates for selective C–H activation of butane. (a) Activity and selectivity of major products of $(M_{0.1}W_{0.4}P_{0.5})O_{2.5+\delta}$ where M = Ru, Rh, or Pd. Rest = summation of all detected products, excluding CO, CO₂, and MAN. (b) Activity and selectivity of minor products of $(M_{0.1}W_{0.4}P_{0.5})O_{2.5+\delta}$, where M = Ru, Rh, or Pd. Reaction conditions: 450 °C, 1 bar, C₄H₁₀/O₂/H₂O = 2:20:3, and 2000 h⁻¹.

surface areas were considered. However, samples calcined at 550 °C revealed much lower consumption rates than the samples calcined at 450 and 700 °C, as shown in Supporting Information Figure S12. To the best of our knowledge, this is the first case of an active and selective catalyst for partial oxidation of *n*-butane without V or Mo.

To obtain further structure–performance relations into $(Ru_{0.1}W_{0.4}P_{0.5})O_{2.5+\delta}$, the product distribution of $(Ru_{0.1}W_{0.4}P_{0.5})O_{2.5+\delta}$ calcined at 450–700 °C is displayed (see Figure 6d). These catalysts showed similar activity and MAN selectivity at 450 °C, 1 bar, C₄H₁₀/O₂/H₂O = 2:20:3, and 2000 h⁻¹. However, more CO and less CO₂ were

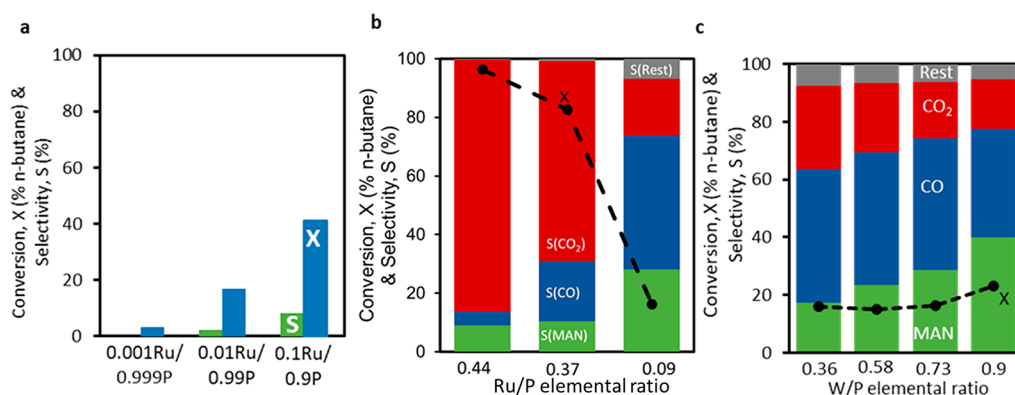


Figure 8. Catalytic performance of supported ruthenium tungsten phosphates for selective C–H activation of butane. (a) Conversion and MAN selectivity of binary Ru/P on SiO₂ with different Ru/P ratios. (b) Conversion and selectivity of major products of Ru/W/P on SiO₂, with decreasing Ru fraction and fixed W/P ratio of 0.77. (c) Conversion and product selectivity Ru/W/P on SiO₂, with fixed 0.05 Ru fraction and varied W/P ratio. Rest = summation of all detected products, excluding CO, CO₂, and MAN. Reaction conditions: 425 °C, 1 bar, C₄H₁₀/O₂/H₂O = 2:20:3, and 2000 h^{−1}.

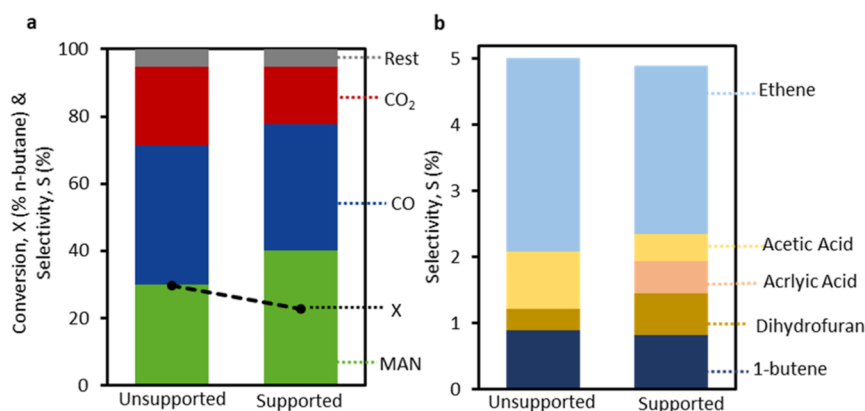


Figure 9. Catalytic performance of unsupported ruthenium tungsten phosphate (ReO₃-related structure) calcined at 550 °C (Concept A) vs supported ruthenium tungsten phosphates (Concept B) containing Ru/W/P = 0.05/0.45/0.5 for selective C–H activation of butane. (a) Activity and distribution of major products. Rest = summation of all detected products, excluding CO, CO₂, and MAN. (b) Distribution of minor products. Reaction conditions: 425 °C, 1 bar, C₄H₁₀/O₂/H₂O = 2:20:3, and 2000 h^{−1}.

produced as byproducts for the catalysts with higher calcination temperatures and crystallinity. Nonetheless, the product spectrum of the rest of the side products was comparable, and the difference in structure appears to have no influence on the selectivity toward alkenes and oxygenates (see Supporting Information Figure S13). This suggests that selective oxidation features of those catalysts are less dependent on structure type and modification of the structure but more sensitive to composition, specifically site isolation, which might have a more significant effect.

The effect of different PGMs, namely, Ru, Rh, and Pd, was also studied, and the results can be found in Figure 7. Rh and Pd tungsten phosphates were also capable of oxidative selective C–H activation. However, Ru-containing catalysts ($S = 25\%$, $X = 47\%$ at $T = 450$ °C) were found to be the most selective, followed by Pd ($S = 16\%$, $X = 37\%$ at $T = 450$ °C) and Rh ($S = 7\%$, $X = 42\%$ at $T = 450$ °C). The trend of *n*-butane consumption decreasing from Ru > Rh > Pd might be reasoned by the same trend regarding the related BET surface areas (see Supporting Information Table S7). From the analysis of minor product spectra, ethene and 1-butene were essential minor products for (Ru_{0.1}W_{0.4}P_{0.5})O_{2.5+δ}, but acetic acid was the most substantial minor product for (Pd_{0.1}W_{0.4}P_{0.5})O_{2.5+δ}. Thus, there may be different reaction

pathways for different PGM tungsten phosphates, and this should be taken into consideration for further development of PGM tungsten phosphates as catalysts for C–H activation.

C–H Activation of Butane: Catalytic Behavior of Supported Ruthenium Tungsten Phosphates. Based on the findings of the positive impact of Ru incorporation into the target structure, efforts to support such materials along the lines of Concept B were pursued. Amorphous supported ruthenium tungsten phosphates were synthesized and investigated. In a first study, Ru dispersed in phosphoric acid supported on silica with different Ru/P ratios have been studied as reference materials (see Figure 8a). While W dispersed in phosphoric acid and phosphoric acid itself on silica were inactive (see Supporting Information Figure S14), dispersed Ru was capable of oxidizing *n*-butane. An increase in Ru loading led to increased activity and MAN selectivity. Almost a MAN selectivity of 10% and a conversion of 43% were obtained for a ratio of 0.1Ru/0.9P. For studying the influence of Ru and W dispersed as a mixture in phosphoric acid, different catalysts with a total weight loading of 35 wt % based on all supported elements in oxide form were synthesized. First, the ratio W/P = 0.77 was constant, and Ru loading varied (see Figure 8b). High Ru fractions in these mixtures led to highly active total oxidation catalysts. The total

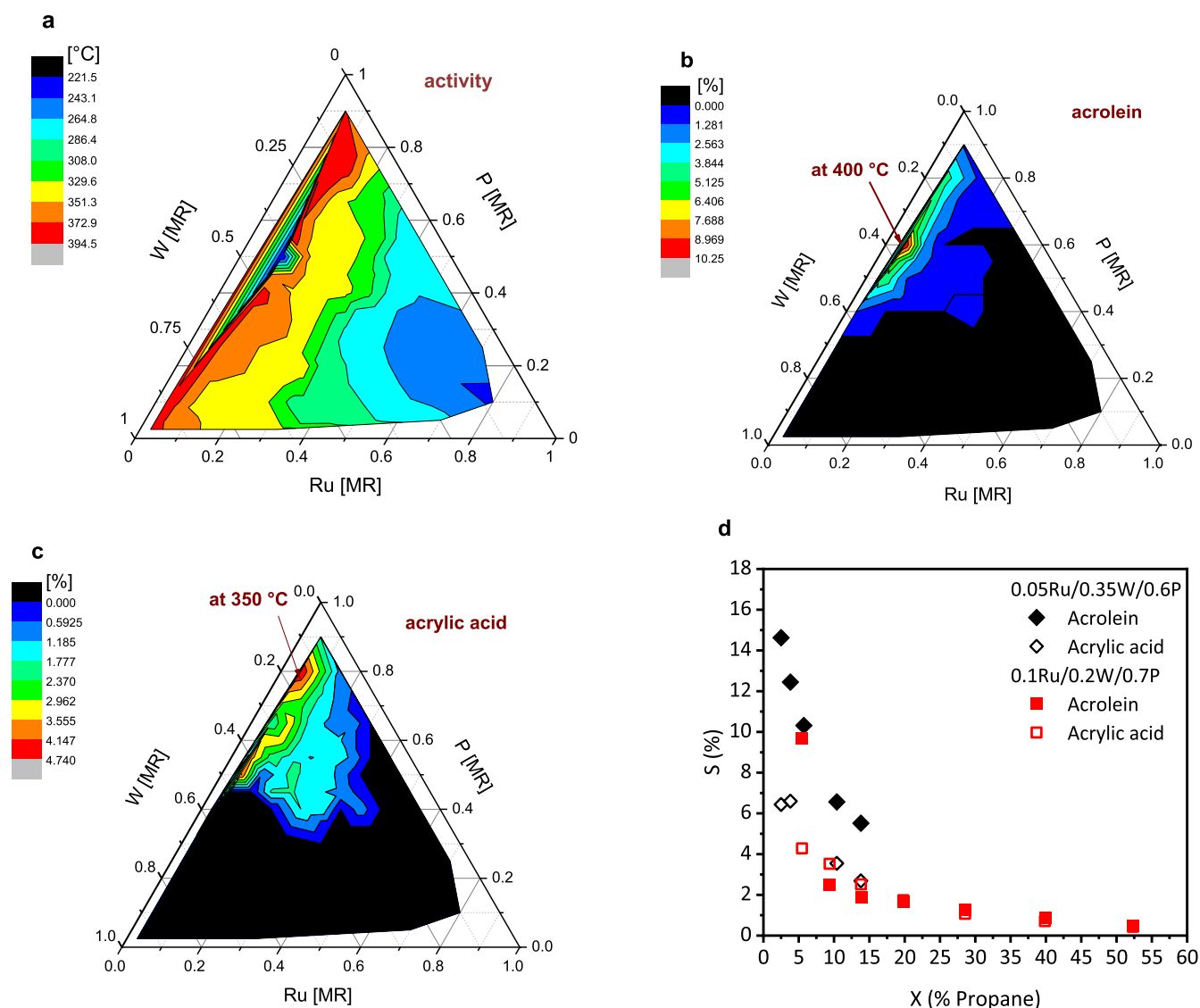


Figure 10. Performance of supported Ru/W/P catalysts for selective C–H activation of propane. (a) Activity of Ru/W/P on SiO₂ represented as T₅₀-values. (b,c) Max. selectivity of acrolein and acrylic acid for X ≥ 10%. (d) Product selectivity of the SiO₂-supported 0.05Ru/0.35W/0.6P and 0.1Ru/0.2W/0.7P. Reaction conditions: 200–400 °C, 3 bar, C₃H₈/O₂/H₂O = 1:15:3, and 3000 h⁻¹.

oxidation behavior at even higher Ru loading was observed over the whole conversion range. The product spectrum of 0.3Ru/0.2W/0.5P at lower butane conversion is included in [Supporting Information Figure S15](#).

In contrast to the binary Ru/P systems (see [Figure 8a](#)), the successive dilution of Ru within the ternary mixtures changed the oxidation behavior from total oxidation to selective oxidation. This catalytic behavior was also observed for much lower conversions measured at a reaction temperature of 375 °C (see [Supporting Information Figure S16](#)). The role of W and the influence of the W/P elemental ratio were determined by keeping the Ru fraction constant (see [Figure 8c](#)). By increasing the W/P ratio, MAN selectivity was improved to 40% at a 23% butane conversion level. The increase of MAN selectivity results from a CO₂ selectivity decrease and indicates that a higher WO₃ content prevents MAN overoxidation.

The catalytic performance of unsupported and supported ruthenium tungsten phosphates with identical Ru/W/P composition is compared in [Figure 9](#). Notable, both catalyst

concepts reveal similar catalytic performance and product distribution. However, it was observed that the supported tungsten phosphate 0.05Ru/0.5W/0.45P had a richer product distribution in C₃ oxygenates with acrylic acid, and the unsupported (Ru_{0.05}W_{0.5}P_{0.45})O_{2.5+δ} with ReO₃-related structure had a slightly higher activity. Remarkably, the BET surface area of the spent unsupported catalyst is 0.7 m²/g, more than 80 times lower than of the supported catalyst (83.6 m²/g). This demonstrates that for both concepts of catalyst synthesis, the dilution of ionic Ru leads to selective oxidation catalysts. An attractive approach is to synthesize supported Ru tungsten phosphates via incipient wetness impregnation. In contrast to the ruthenium tungsten phosphates with a ReO₃-related structure, the whole Ru/W/P composition range, even including promoters, can be studied. The benchmark catalyst VPP reaches a conversion of 95% and a MAN selectivity of 66%⁵⁵ at similar reaction conditions (420 °C, 1 bar, C₄H₁₀/O₂/H₂O = 2:20:3 and 2000 h⁻¹). This indicates the potential for the optimization of the presented novel catalysts themselves

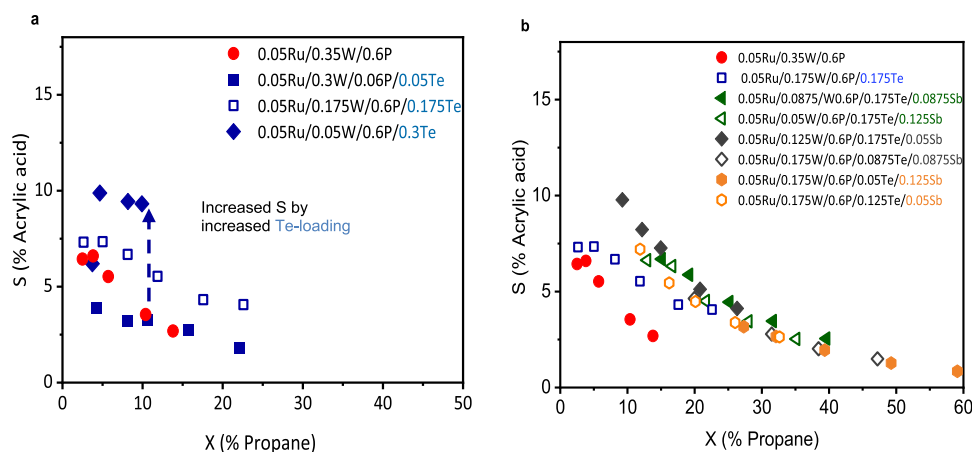


Figure 11. Performance of supported Ru/W/P/Te and Ru/W/P/Te/Sb catalysts for selective C–H activation of propane. (a) Acrylic acid selectivity of the SiO₂-supported Ru/W/P/Te candidates in comparison to 0.05Ru/0.35W/0.6P. (b) Acrylic acid selectivity of the SiO₂-supported Ru/W/P/Te/Sb candidates in comparison to 0.05Ru/0.35W/0.6P and 0.05Ru/0.175W/0.6P/0.175Te. Reaction conditions: 200–400 °C, 3 bar, C₃H₈/O₂/H₂O = 1:15:3, and 3000 h^{−1}.

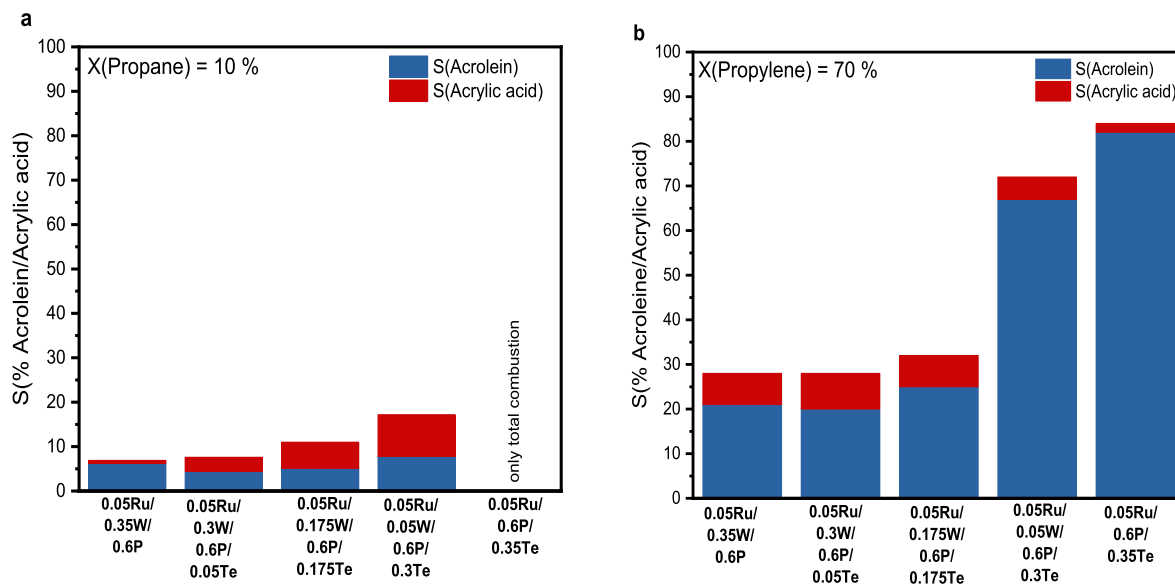


Figure 12. Performance of supported Ru/W/P/Te for selective C–H activation of propane and propylene. (a) Acetic acid and acrolein selectivity of propane oxidation at iso-conversion condition: X = 10%. (b) Acrylic acid and acrolein selectivity of propylene oxidation at iso-conversion condition: X = 70%. Reaction conditions: 200–400 °C, 3 bar, C₃/O₂/H₂O = 1:15:3, and 3000 h^{−1}.

but also adaptations regarding reaction conditions may be feasible.

C–H Activation of Propane and Propylene: Extensive Composition and Promoter Study. The catalytic performance data were accumulated at 200–400 °C, 3 bar, C₃/O₂/H₂O = 1:15:3, and 3000 h^{−1}. For propane conversion, 109 SiO₂-supported phosphates, consisting of Ru and W dispersed in phosphoric acid, were prepared considering the whole Ru/W/P-ternary composition diagram. Figure 10a–c presents an overview of the catalytic performance of all materials, while Figure 10d focuses on two catalysts in more detail. In Figure 10a, the catalytic activity is represented as T₅₀-values, suggesting the temperature required to achieve 50% propane conversion. With an increasing Ru loading, the activity increased, while simultaneously the selectivity of acrolein and acrylic acid dropped, as can be seen in 10b,c. Both oxygenates were only formed at low Ru and medium or high P loadings with a maximum at a Ru-fraction of 0.05, respectively. A

maximum summed yield of acrolein and acrylic acid of 1.12% (X: 13.8%, S(acrolein) = 5.5%, S(acrylic acid) = 2.7%) was observed for 0.05Ru/0.35W/0.6P. The performance data is represented in Figure 10d in comparison to 0.1Ru/0.2W/0.7P, which shows due to a higher Ru loading an enormously increased activity but a drop in selectivity toward carboxylic C₃-oxygenates. The prevention of overoxidation might also be the reason for an increased summed selectivity of organic oxygenates. Besides acrolein and acrylic acid, the byproducts were produced: acetic acid, ethylene, acetaldehyde, and propylene. The complete product spectrum of both catalysts can be found in Supporting Information Figure S17. Below Ru-fractions of 0.05, the catalysts were inactive at the applied conditions. W-free SiO₂-supported Ru/P-catalysts were highly active for Ru/P-ratios of 1/0 to 1/3, leading primarily to total propane combustion. Small amounts of CO and acetic acid were identified for Ru/P-ratios of 1/3 (Supporting Information Figure S18). Foppa et al.⁵⁶ used the high-throughput data set

of these 109 catalysts and their catalytic results as the target for the subgroup discovery (SGD) artificial intelligence approach. They combined the experimental results with theoretical data sets from DFT calculations and could identify that temperature, phosphorous, composition-weighted electronegativity are critical parameters in order to achieve high yields of acrolein and acrylic acid.

The performance of 0.05Ru/0.35W/0.6P was improved by adding a fourth component in dependence of the W loading. In this context, Te had the strongest impact on selectivity, especially on acrylic acid. With increasing Te loading, the selectivity could be increased by up to 5% (see Figure 11a). Unfortunately, too high Te loadings resulted in a strong activity drop by 50%. To overcome this problem, Sb was added as an activity promoter giving five-component Ru/W/P/Te/Sb catalysts, showing an improved activity of up to 40%. For conversions lower than 25%, the addition of Sb also led to higher selectivity (up to +6.5%). After the 25% conversion threshold, all five-component catalysts followed the same conversion/selectivity curve independent of the concrete elemental W, Te, and Sb loading (see Figure 11b). Te-free Ru/W/P/Sb catalysts were very active but not selective toward acrolein or acrylic acid ($X = 26.4\%$ and $S(\text{acrolein}) = 9.4\%$ and $S(\text{acrylic acid}) = 3.0\%$). Bragg reflections in XRPD could be assigned to TeO_3 with molar fractions of at least 0.3 (see Supporting Information Figure S4). However, these spent catalysts were completely XRD amorphous (see Supporting Information Figure S5).

The catalytic performance data for propylene oxidation compared with the propane data showed significantly higher activity and selectivity (see Figure 12), emphasizing the critical role of tungsten during the first C–H activation. While the catalyst 0.05Ru/0.35W/0.6P reached a maximal combined yield of 1.12% for acrolein and acrylic acid in propane oxidation ($X: 13.8\%$, $S(\text{acrolein}) = 5.5\%$, $S(\text{acrylic acid}) = 2.7\%$), a combined yield of 20% could be achieved in propylene oxidation ($X: 83.3\%$, $S(\text{acrolein}) = 18.0\%$, $S(\text{acrylic acid}) = 6.1\%$). This performance could even be surpassed by the W-free system 0.05Ru/0.35Te/0.6P with a maximum combined yield of 61% in propylene oxidation ($X: 72.5\%$, $S(\text{acrolein}) = 81.8\%$, $S(\text{acrylic acid}) = 2.5\%$). Only in W-free catalyst systems, the total oxidation behavior for propane was observed.

CONCLUSIONS

By adopting two different synthesis concepts, we were able to present in this paper new PGM tungsten phosphate catalyst candidates for lower alkane oxidation to oxygenates. These nanostructured phases enable the homogeneous distribution of ruthenium oxide active sites over a wide compositional range. The dilution of the PGMs such as Ru prevents overoxidation of intermediates and leads to selective oxidation of lower alkanes to oxygenates. As far as we are aware, Ru/W/P/O catalysts prove for the first time that heterogeneous catalysts, without V or Mo in their structure, were active, stable, and respectably selective for the direct conversion of propane and butane to oxygenates. By focusing on *n*-butane oxidation to MAN, the unsupported catalysts, synthesized via SCS and modified by different calcination temperatures (Concept A), led to the hypothesis that rather the Ru/W/P composition is essential and not the degree of crystallinity. This conclusion made the development of Concept B indispensable: Diluting Ru-based active sites through the synthesis of XRD-amorphous

ruthenium tungsten phosphates supported on SiO_2 . This approach enables the study over the whole PGM/W/P composition range, including promoters. Findings of synthesis Concept B confirmed our hypothesis since XRD-amorphous supported Ru/W/P catalysts showed similar performance for *n*-butane oxidation (referring to conversion and MAN selectivity) as their analogue crystalline unsupported catalysts. Both synthesis approaches led to homogeneous elemental distribution of Ru, W, and P with a polycrystalline nanoparticulate morphology. While for the unsupported $(\text{Ru}_{0.1}\text{W}_{0.4}\text{P}_{0.5})\text{O}_{2.5+\delta}$ catalyst, a ReO_3 -related structure could be explicitly proved, there are at least strong indications that supported ruthenium tungsten phosphates may adopt a ReO_3 -related structure as well. At 425°C , 1 bar, $\text{C}_4\text{H}_{10}/\text{O}_2/\text{H}_2\text{O} = 2:20:3$ vol %, and 2000 h^{-1} , the best-tested material regarding MAN selectivity, 0.05Ru/0.45W/0.5P supported on SiO_2 , showed 40% MAN selectivity at 21% *n*-butane conversion. While Ru, together with phosphates, was capable of oxidizing unselectively *n*-butane, the addition of W was proven to be crucial in suppressing the total oxidation of oxygenates to CO_2 . In the unsupported PGM tungsten phosphates, W is required to stabilize the bulk crystal structure. Descriptors (site isolation, redox-active metal oxide, and phosphate host structure) from heterogeneous and homogeneous catalysis were considered and employed to design these PGM tungsten phosphates. Thus, the approach reported here can be a bridge between both research areas. This work opens a wide field for research in catalytic materials, but it also has a substantial impact on catalytic applications and resource efficiency. Nevertheless, the elucidation of the active site, particularly the role and local structures of the materials with ReO_3 -related structure for C–H activation of lower alkanes in the PGM tungsten phosphates, remains a crucial question and advanced characterization and theoretical calculations are advocated.

METHODS

Synthesis of Unsupported PGM Tungsten Phosphates. Unsupported PGM tungsten phosphates were synthesized with the solution combustion technique.^{29,57} The precursors consisting of $\text{Ru}(\text{NO}) (\text{NO}_3)_3$ (Alfa Aesar, min. 31.3% Ru), $(\text{NH}_4)_6\text{W}_{12}\text{O}_{39} \cdot x\text{H}_2\text{O}$ (Alfa Aesar, p.a.), $(\text{NH}_4)_2\text{HPO}_4$ (VWR Chemicals, p.a.) were dissolved in deionized water with a minimal amount of HNO_3 and glycine (metal-to-glycine ratio 1:3). $\text{Rh}(\text{NO}_3)_3$ (Umicore, 35.28% Rh) or $\text{Pd}(\text{NO}_3)_2$ (Umicore, 40.440% Pd) were used instead of $\text{Ru}(\text{NO})(\text{NO}_3)_3$ for the synthesis of the respective PGM tungsten phosphates. The solution was then heated to 70°C to form a gel, and it was subsequently placed into a furnace at 400°C , at which ignition and combustion occurred. The solid product was then calcined at different temperatures, that is, no calcination, 450, 550, 700, and 900°C , and duration to obtain a different degree of crystallinity. The materials were named $(\text{Ru}_{0.1}\text{W}_{0.4}\text{P}_{0.5})\text{O}_{2.5+\delta}$ for the elemental composition, followed by the calcination temperature, for example, $(\text{Ru}_{0.1}\text{W}_{0.4}\text{P}_{0.5})\text{O}_{2.5+\delta}$ at 550°C .

Synthesis of Supported Ruthenium Tungsten Phosphates. Supported ruthenium tungsten phosphates were synthesized by incipient wetness impregnation. Dry SiO_2 (5 g, 500–1000 μm , CARIAC Q20C Silica Fuji Silysia) was impregnated according to the desired elemental composition and with a total elemental loading of 35 wt % with a mixture of the different solutions: RuCl_3 (3.24 M in 18 M HCl, Umicore), H_3PO_4 (phosphoric acid, 10 M in H_2O , Acros Organics),

(NH₄)₆H₂W₁₂O₄₀ hydrate (0.1 M in H₂O, HC Stark), Te(OH)₆ (telluric acid, 1 M in H₂O, Sigma-Aldrich), Sb(CH₃COO)₃ (1 M in 4 M tartaric acid, C₄H₆O₆, Sigma-Aldrich), and C₁₀H₂₅O₅Ta (tantalum ethanolate, 99.9%, Sigma-Aldrich). Typical batch sizes for the impregnation were adapted for 5 g of silica support material, which was distributed as a shallow bed of a thickness of less than 3 mm in a porcelain dish. The support material was then wetted with the impregnation solution containing the mixture of all elements to be deposited. The impregnation procedure was carried out allowing all liquid to be adsorbed by the carrier material with no supernatant liquid at any time during the process. Impregnated materials were allowed to stand for 20 min before submitting to drying conditions. The impregnated materials were then dried at 80 °C for 16 h.

Bulk Structure Characterization. XRD patterns were measured in Bragg–Brentano (reflection) geometry on a Bruker AXS D8 Advance II diffractometer (i.e., Cu K α_{1+2} radiation, Ni filter, energy-dispersive position-sensitive LynxEye silicon strip detector). The sample powder was filled into the recess of a cup-shaped sample holder, the surface of the powder bed being flush with the sample holder edge (front loading). The powder XRD data were analyzed using a full pattern fitting, according to the Rietveld method as implemented in the TOPAS software [TOPAS version 5, copyright 1999–2014 Bruker AXS].

N₂ physisorption was carried out using an Autosorb-6-B, Quantachrome at the temperature of liquid N₂. The sample was degassed under dynamic vacuum at 423 K for 2 h prior to physisorption. Full adsorption–desorption isotherms were recorded. The specific surface area according to the BET method was calculated from the linear range of the adsorption isotherm ($p/p_0 = 0.05–0.3$).

Elemental Analysis. C, H, N, and S elemental analysis was performed with a Thermo FlashEA 1112 Organic Elemental Analyzer, and the measurement method was dynamic flash combustion (modified Dumas method) at 1020 °C. All catalysts were characterized before and after catalytic testing.

An ICP-OES Optima 8300 PerkinElmer with Zyktron nebulizer was applied for analysis of W/Ru/P elemental composition. Calibration is based on certified, commercially available standard solutions, WF₆-complex, RuCl₃, and K₂HPO₄. Around 20–30 mg of the samples were dissolved in acidic solution in an Anton Paar Multiwave Pro autoclave at 220 °C and 6 MPa. The medium for dissolution consisted of 4 mL of nitric acid (65%) Suprapur, 2 mL of perchloric acid (70%) Suprapur, 1 mL of hydrofluoric acid (40%) Suprapur, and 1 mL of hydrochloric acid (32%) p.a. After dissolution, autoclave solutions are filled up to 50 mL by water (0.05 μ S/cm). Aliquots were taken and filled up to 10 mL by water for ICP-OES analysis. Volumes of aliquots were 1000 μ L series (a) and 300 μ L series (b).

Thermal Analysis. Thermogravimetric and evolved gas analysis was carried out on a NETZSCH STA 449C Jupiter thermoanalyzer equipped with an electromagnetic microbalance with top loading. A highly sensitive sample carrier with Pt/Pt–Rh disc-shaped thermocouples was used. Measurements were taken in the temperature range of 40–1000 °C under a controlled Ar/O₂ flow of 79:21 mL_n/min with a heating rate of 5°/min. The controlled gas flow was maintained with mass flow controllers EL-Flow by Bronkhorst, additionally calibrated with a flow meter Definer 220. Gases used in the experiments were Ar (99.999%) and O₂ (99.999%)

purified with additional OxySorb and Hydrosorb cartridges. Samples of 10 mg were positioned into corundum crucibles (85 μ L) without lids. Temperatures were calibrated against the melting points of In, Sn, Bi, Zn, Pb, Al, and Au. The evolved gases were monitored with a quadrupole mass spectrometer (QMS200 Omnistar, Pfeiffer Vacuum) coupled to STA via a quartz capillary (ID-0.15 mm) heated to 120 °C. The experiments were performed with an electron ionization energy of 60 eV and a dwell time per mass of 0.2 s. The main mass gates used were m/z 18 (H₂O), 28 (CO), 30 (NO), 32 (O₂), 44 (CO₂), and 46 (NO₂). The Proteus Thermal Analysis program was used for processing the raw data.

Transmission Electron Microscopy. The structure and morphology of the as-grown nanostructures were examined using an FEI Talos F200X transmission electron microscope operating at 200 kV equipped with an energy-dispersive X-ray spectroscopy (EDS) system to allow for the elemental analysis of the observed features. High-resolution transmission electron microscopy (HRTEM) images were taken on an aberration-corrected JEOL JEM-ARM200F TEM equipped with a high-angle silicon EDS detector. Selected area electron diffraction (SAED) and fast Fourier transform (FFT) patterns were also acquired in order to extract structural information from the sample. In addition, high-resolution HAADF-STEM images based on Z-contrast imaging and corresponding STEM-EDS analysis were accomplished to determine the elemental composition of the nanomaterial. For the TEM observations, the powder sample was deposited on a carbon lacey Cu grid. The recorded signal of Cu in the acquired EDS spectra arises from the used lacey carbon Cu grid. The presence of the carbon signal is due to contamination of the sample with carbon during its synthesis and/or the supported Cu TEM grid. The occasional detection of Al and Mg in the EDS spectra is related to impurities in the sample TEM holder.

Catalyst Tests for Selective C–H Activation of Butane. A high-throughput eight parallel fixed-bed reactor setup from GmbH was used as described by Schulz et al.³⁰ Each reactor was loaded with 1 mL of catalyst (100–200 μ m unsupported PGM tungsten phosphate or 500–1000 μ m supported PGM phosphate) in the isothermal zone, and the remaining dead volume in the reactor was filled with the inert material (calcined corundum, 400–700 μ m, CeramTec). The catalysts were first conditioned at 1 bar and 300 °C (10 °C/min) in dilute O₂ flow (5 vol % O₂, 95 vol % N₂, and 2000 h^{–1}) for 2 h. The dilute O₂ flow was then switched to the reactant feed flow (C₄H₁₀/O₂/H₂O/Ar/N₂ = 2:20:3:2:73, 2000 h^{–1}) for 16 h. Subsequently, the reaction temperature was increased to 375 °C. After an initial equilibration period of 30 min, the catalytic measurements were started. The standard testing procedure includes 5 GC analyses per reactor and temperature, with the reactor temperature ramping up in 25 °C (2 °C/min) steps up to a maximum temperature of 450 °C, followed by ramping down to 350 °C. Finally, the reactors were cooled down to ambient temperature in dilute O₂ flow (5 vol % O₂, 95 vol % N₂, and 2000 h^{–1}). Definitions and calculations of the selectivity, *S*, and activity, *X*, expressed as C₄H₁₀ conversion are included as [Supporting Information Methods](#). Carbon balances were always 100 \pm 3%.

Catalyst Tests for Selective C–H Activation of Propane and Propylene. All materials were tested in a 48-fold high-throughput setup from GmbH. Each reactor was loaded with 1 mL of catalyst in a 0.5–1 mm sized fraction. The detailed test procedure can be found in refs 58 and 59.

Calcined corundum (0.4–0.7 mm, CeramTec) was used as the inert material below and above the catalyst bed. The standard testing conditions involved temperature changes between 200 and 400 °C (50 °C steps), 3 bar, and a gas feed composition of propane/propylene 1 vol %, O₂ 15 vol %, H₂O 3 vol %, Ar 3 vol %, and N₂ as the balance at a fixed GHSV of 3000 h⁻¹. Typically, conditions were repeated several times to test the stability of the catalyst performance under the given conditions. The data evaluation was performed using the commercial software tool myhte.

■ ASSOCIATED CONTENT

■ Supporting Information

The Supporting Information is available free of charge at <https://pubs.acs.org/doi/10.1021/acscatal.2c02645>.

TG-MS analysis, XRPD patterns, results of Rietveld fitting, XRD analysis, elemental analysis, Rietveld refinement, XPS spectra, consumption rate, catalytic performance, activity and product selectivity, conversion and selectivity, product distribution, list of unsupported PGM phosphates, list of fresh unsupported (Ru_{0.1}W_{0.4}P_{0.5})O_{2.5}+δ, list of spent unsupported (Ru_{0.1}W_{0.4}P_{0.5})O_{2.5}+δ, list of all studied supported PGM phosphates, selected fresh and spent unsupported (Ru_{0.1}W_{0.4}P_{0.5})O_{2.5}+δ, measured lattice d-spacings, BET surface areas, and XPS analysis (PDF)

■ AUTHOR INFORMATION

Corresponding Author

Stephan A. Schunk – hte GmbH, 69123 Heidelberg, Germany; BASF SE, Process Research and Chemical Engineering, 67056 Ludwigshafen, Germany; Institute of Chemical Technology, Universität Leipzig, 04103 Leipzig, Germany; orcid.org/0000-0002-1253-4566; Phone: +49-6221-7497-0; Email: stephan.schunk@hte-company.de

Authors

Rhea Machado – BasCat-UniCat BASF JointLab, Technische Universität Berlin, 10623 Berlin, Germany

Maria Dimitrakopoulou – Fritz Haber Institute of the Max Planck Society, 14195 Berlin, Germany

Frank Girgsdies – Fritz Haber Institute of the Max Planck Society, 14195 Berlin, Germany

Patricia Löser – hte GmbH, 69123 Heidelberg, Germany

Jingxiu Xie – BasCat-UniCat BASF JointLab, Technische Universität Berlin, 10623 Berlin, Germany; Present Address: Chemical Technology, University of Groningen, 9747 AG Groningen, the Netherlands

Knut Wittich – hte GmbH, 69123 Heidelberg, Germany

Markus Weber – Institute for Inorganic Chemistry, Rheinische Friedrich-Wilhelms-Universität, 53121 Bonn, Germany

Michael Geske – BasCat-UniCat BASF JointLab, Technische Universität Berlin, 10623 Berlin, Germany

Robert Glaum – Institute for Inorganic Chemistry, Rheinische Friedrich-Wilhelms-Universität, 53121 Bonn, Germany;

orcid.org/0000-0001-5805-1466

Alexander Karbstein – Institute for Inorganic Chemistry, Rheinische Friedrich-Wilhelms-Universität, 53121 Bonn, Germany

Frank Rosowski – BasCat-UniCat BASF JointLab, Technische Universität Berlin, 10623 Berlin, Germany; BASF

SE, Process Research and Chemical Engineering, 67056

Ludwigshafen, Germany

Sven Titlbach – BASF SE, Process Research and Chemical Engineering, 67056 Ludwigshafen, Germany

Katarzyna Skorupska – Fritz Haber Institute of the Max Planck Society, 14195 Berlin, Germany; orcid.org/0000-0002-1970-0395

Andrey V. Tarasov – Fritz Haber Institute of the Max Planck Society, 14195 Berlin, Germany

Robert Schlögl – Fritz Haber Institute of the Max Planck Society, 14195 Berlin, Germany

Complete contact information is available at:

<https://pubs.acs.org/doi/10.1021/acscatal.2c02645>

■ Notes

The authors declare no competing financial interest.

The data sets generated during and/or analyzed during the current study are available from the corresponding author on reasonable request.

■ ACKNOWLEDGMENTS

J. Allan (FHI), M. Hashagen (FHI), O. Timpe (FHI), and J. Krone (TU Berlin) are acknowledged for the TG–MS, XRD, N₂ physisorption, ICP-OES, and C, H, N, and S elemental analysis, respectively. Sabine Hirth (BASF SE) is acknowledged for her work on XPS measurements and interpretation.

■ REFERENCES

- (1) Dieterle, M.; Schwab, E. Raw Material Change in the Chemical Industry. *Top. Catal.* **2016**, *59*, 817–822.
- (2) Deshlahra, P.; Iglesia, E. Reactivity and Selectivity Descriptors for the Activation of C–H Bonds in Hydrocarbons and Oxygenates on Metal Oxides. *J. Phys. Chem. C* **2016**, *120*, 16741–16760.
- (3) Latimer, A. A.; Kulkarni, A. R.; Aljama, H.; Montoya, J. H.; Yoo, J. S.; Tsai, C.; Abild-Pedersen, F.; Studt, F.; Nørskov, J. K. Understanding trends in C–H bond activation in heterogeneous catalysis. *Nat. Mater.* **2017**, *16*, 225–229.
- (4) Zhang, J.; Liu, X.; Blume, R.; Zhang, A.; Schlögl, R.; Su, D. S. Surface-modified carbon nanotubes catalyze oxidative dehydrogenation of n-butane. *Science* **2008**, *322*, 73–77.
- (5) Grant, J. T.; Carrero, C. A.; Goeltz, F.; Venegas, J.; Mueller, P.; Burt, S. P.; Specht, S. E.; McDermott, W. P.; Chieragato, A.; Hermans, I. Selective oxidative dehydrogenation of propane to propene using boron nitride catalysts. *Science* **2016**, *354*, 1570–1573.
- (6) Leckie, L.; Mapolie, S. F. Triazole complexes of ruthenium immobilized on mesoporous silica as recyclable catalysts for octane oxidation. *Catal. Commun.* **2019**, *131*, 105803.
- (7) Labinger, J. A. Selective alkane oxidation: hot and cold approaches to a hot problem. *J. Mol. Catal. A: Chem.* **2004**, *220*, 27–35.
- (8) Miller, J. H.; Bui, L.; Bhan, A. Pathways, mechanisms, and kinetics: a strategy to examine byproduct selectivity in partial oxidation catalytic transformations on reducible oxides. *React. Chem. Eng.* **2019**, *4*, 784–805.
- (9) Schlögl, R. Selective Oxidation: From a Still Immature Technology to the Roots of Catalysis Science. *Top. Catal.* **2016**, *59*, 1461–1476.
- (10) Grasselli, R. K. Fundamental Principles of Selective Heterogeneous Oxidation Catalysis. *Top. Catal.* **2002**, *21*, 79–88.
- (11) López Nieto, J. M.; Solsona, B. Gas phase heterogeneous partial oxidation reactions. *Metal Oxides in Heterogeneous Catalysis*; Elsevier, 2018; pp 211–286.
- (12) Schunk, S. A. Oxyfunctionalization of Alkanes. In *Handbook of Heterogeneous Catalysis*; Ertl, G., Knözinger, H., Schth, F., Weitkamp, J., Eds.; Wiley-VCH Verlag GmbH & Co. KGaA, 2008.
- (13) Bielański, A.; Haber, J. *Oxygen in Catalysis*; M. Dekker, 1991.

- (14) Ballarini, N.; Cavani, F.; Cortelli, C.; Ligi, S.; Pierelli, F.; Trifirò, F.; Fumagalli, C.; Mazzoni, G.; Monti, T. VPO catalyst for n-butane oxidation to maleic anhydride: A goal achieved, or a still open challenge? *Top. Catal.* **2006**, *38*, 147–156.
- (15) Trifirò, F.; Grasselli, R. K. How the Yield of Maleic Anhydride in n-Butane Oxidation, Using VPO Catalysts, was Improved Over the Years. *Top. Catal.* **2014**, *57*, 1188–1195.
- (16) Glaum, R.; Welker-Nieuwoudt, C.; Dobner, C.-K.; Eichelbaum, M.; Gruchow, F.; Heine, C.; Karpov, A.; Kniep, R.; Rosowski, F.; Schlögl, R.; Schunk, S. A.; Titlbach, S.; Trunschke, A. Resource-Efficient Alkane Selective Oxidation on New Crystalline Solids: Searching for Novel Catalyst Materials. *Chem. Ing. Tech.* **2012**, *84*, 1766–1779.
- (17) Botella, P.; López Nieto, J. M.; Solsona, B.; Mifsud, A.; Márquez, F. The Preparation, Characterization, and Catalytic Behavior of MoVTeNbO Catalysts Prepared by Hydrothermal Synthesis. *J. Catal.* **2002**, *209*, 445.
- (18) Hävecker, M.; Wrabetz, S.; Kröhnert, J.; Csepei, L.-I.; Naumann d'Alnoncourt, R.; Kolen'ko, Y. V.; Girgsdies, F.; Schlögl, R.; Trunschke, A. Surface chemistry of phase-pure M1 MoVTeNb oxide during operation in selective oxidation of propane to acrylic acid. *J. Catal.* **2012**, *285*, 48.
- (19) Lin, M. M. Selective oxidation of propane to acrylic acid with molecular oxygen. *Appl. Catal., A* **2001**, *207*, 1.
- (20) Melzer, D.; Xu, P.; Hartmann, D.; Zhu, Y.; Browning, N. D.; Sanchez-Sanchez, M.; Lercher, J. A. Inside Cover: Atomic-Scale Determination of Active Facets on the MoVTeNb Oxide M1 Phase and Their Intrinsic Catalytic Activity for Ethane Oxidative Dehydrogenation (Angew. Chem. Int. Ed. 31/2016). *Angew. Chem., Int. Ed.* **2016**, *55*, 8770.
- (21) Ushikubo, T.; Oshima, K.; Kayou, A.; Vaarkamp, M.; Hatano, M. Ammoxidation of Propane over Catalysts Comprising Mixed Oxides of Mo and V. *J. Catal.* **1997**, *169*, 394–396.
- (22) Seshan, K. Commercial process for acrylonitrile from propane. *Appl. Catal.* **1990**, *67*, N5.
- (23) Thorsteinson, E. M.; Wilson, T. P.; Young, F. G.; Kasai, P. H. The oxidative dehydrogenation of ethane over catalysts containing mixed oxides of molybdenum and vanadium. *J. Catal.* **1978**, *52*, 116–132.
- (24) Cheng, M.-J.; Goddard, W. A. The critical role of phosphate in vanadium phosphate oxide for the catalytic activation and functionalization of n-butane to maleic anhydride. *J. Am. Chem. Soc.* **2013**, *135*, 4600–4603.
- (25) Cheng, M.-J.; Goddard, W. A.; Fu, R. The Reduction-Coupled Oxo Activation (ROA) Mechanism Responsible for the Catalytic Selective Activation and Functionalization of n-Butane to Maleic Anhydride by Vanadium Phosphate Oxide. *Top. Catal.* **2014**, *57*, 1171–1187.
- (26) Roy, S. C. Thermodynamically stable and metastable solids: New approaches to the synthesis of anhydrous phosphates containing vanadium, molybdenum, and/or tungsten. Dissertation; Rheinische Friedrich-Wilhelms-Universität Bonn: Bonn, 2015.
- (27) Roy, S. C.; Raguz, B.; Assenmacher, W.; Glaum, R. Synthesis and crystal structure of mixed metal(III) tungsten(VI) orthorhombic phosphates. *Solid State Sci.* **2015**, *49*, 18–28.
- (28) Hegde, M. S.; Madras, G.; Patil, K. C. Noble metal ionic catalysts. *Acc. Chem. Res.* **2009**, *42*, 704–712.
- (29) Varma, A.; Mukasyan, A. S.; Rogachev, A. S.; Manukyan, K. V. Solution Combustion Synthesis of Nanoscale Materials. *Chem. Rev.* **2016**, *116*, 14493–14586.
- (30) Schulz, C.; Roy, S. C.; Wittich, K.; d'Alnoncourt, R. N.; Linke, S.; Stempel, V. E.; Frank, B.; Glaum, R.; Rosowski, F. α II-(VI-W)OPO₄ catalysts for the selective oxidation of n-butane to maleic anhydride. *Catal. Today* **2019**, *333*, 113–119.
- (31) Welker-Nieuwoudt, C.; Rosowski, F.; Goebel, M.; Glaum, R.; Subrata, C. R.; Hautier, G.; Waroquiers, D.; Naumann d'Alnoncourt, R.; Stempel, V. E.; Linke, S. Wolframphosphat der ReO₃-Strukturfamilie: Offenlegungsschrift. DE 102016007628 A1, 2016.
- (32) Li, X.; Lunkenbein, T.; Pfeifer, V.; Jastak, M.; Nielsen, P. K.; Girgsdies, F.; Knop-Gericke, A.; Rosowski, F.; Schlögl, R.; Trunschke, A. Selective Alkane Oxidation by Manganese Oxide: Site Isolation of MnOx Chains at the Surface of MnWO₄ Nanorods. *Angew. Chem., Int. Ed.* **2016**, *55*, 4092–4096.
- (33) Choudhary, T. V.; Banerjee, S.; Choudhary, V. Catalysts for combustion of methane and lower alkanes. *Appl. Catal., A* **2002**, *234*, 1–23.
- (34) Petrov, A. W.; Ferri, D.; Kröcher, O.; van Bokhoven, J. A. Design of Stable Palladium-Based Zeolite Catalysts for Complete Methane Oxidation by Postsynthesis Zeolite Modification. *ACS Catal.* **2019**, *9*, 2303–2312.
- (35) Wang, P.; Fu, G.; Wan, H. How High Valence Transition Metal Spreads Its Activity over Nonmetal Oxo: A Proof-of-Concept Study. *ACS Catal.* **2017**, *7*, 5544–5548.
- (36) Zhang, F.; Pan, L.; Choi, J.; Mehar, V.; Diulus, J. T.; Asthagiri, A.; Weaver, J. F. Propane σ -Complexes on PdO(101): Spectroscopic Evidence of the Selective Coordination and Activation of Primary C-H Bonds. *Angew. Chem., Int. Ed.* **2015**, *54*, 13907–13911.
- (37) Martin, R.; Kim, M.; Asthagiri, A.; Weaver, J. F. Alkane Activation and Oxidation on Late-Transition-Metal Oxides: Challenges and Opportunities. *ACS Catal.* **2021**, *11*, 4682–4703.
- (38) Sushma; Kumari, M.; Saroha, A. K. Performance of various catalysts on treatment of refractory pollutants in industrial wastewater by catalytic wet air oxidation: A review. *J. Environ. Manag.* **2018**, *228*, 169–188.
- (39) Barbier, J.; Oliviero, L.; Renard, B.; Duprez, D. Role of ceria-supported noble metal catalysts (Ru, Pd, Pt) in wet air oxidation of nitrogen and oxygen containing compounds. *Top. Catal.* **2005**, *33*, 77–86.
- (40) Periana, R. A.; Taube, D. J.; Gamble, S.; Taube, H.; Fujii, H. Platinum catalysts for the high-yield oxidation of methane to a methanol derivative. *Science* **1998**, *280*, 560–564.
- (41) Palkovits, R.; Antonietti, M.; Kuhn, P.; Thomas, A.; Schüth, F. Solid catalysts for the selective low-temperature oxidation of methane to methanol. *Angew. Chem., Int. Ed.* **2009**, *48*, 6909–6912.
- (42) Shan, J.; Li, M.; Allard, L. F.; Lee, S.; Flytzani-Stephanopoulos, M. Mild oxidation of methane to methanol or acetic acid on supported isolated rhodium catalysts. *Nature* **2017**, *551*, 605–608.
- (43) Kwon, Y.; Kim, T. Y.; Kwon, G.; Yi, J.; Lee, H. Selective Activation of Methane on Single-Atom Catalyst of Rhodium Dispersed on Zirconia for Direct Conversion. *J. Am. Chem. Soc.* **2017**, *139*, 17694–17699.
- (44) Tang, Y.; Li, Y.; Fung, V.; Jiang, D.-E.; Huang, W.; Zhang, S.; Iwasawa, Y.; Sakata, T.; Nguyen, L.; Zhang, X.; Frenkel, A. I.; Tao, F. F. Single rhodium atoms anchored in micropores for efficient transformation of methane under mild conditions. *Nat. Commun.* **2018**, *9*, 1231.
- (45) Taccardi, N.; Grabau, M.; Debuschewitz, J.; Distaso, M.; Brandl, M.; Hock, R.; Maier, F.; Papp, C.; Erhard, J.; Neiss, C.; Peukert, W.; Görling, A.; Steinrück, H.-P.; Wasserscheid, P. Gallium-rich Pd-Ga phases as supported liquid metal catalysts. *Nat. Chem.* **2017**, *9*, 862–867.
- (46) Vajda, S.; Pellin, M. J.; Greeley, J. P.; Marshall, C. L.; Curtiss, L. A.; Ballentine, G. A.; Elam, J. W.; Catillon-Mucherie, S.; Redfern, P. C.; Mehmood, F.; Zapol, P. Subnanometre platinum clusters as highly active and selective catalysts for the oxidative dehydrogenation of propane. *Nat. Mater.* **2009**, *8*, 213–216.
- (47) Inoue, T.; Asakura, K.; Iwasawa, Y. Characterization of Pt/SbOx Catalysts Active for Selective Oxidation of Isobutane by Means of XRD, TEM, and XAFS. *J. Catal.* **1997**, *171*, 457–466.
- (48) Inoue, T.; Oyama, S.; Imoto, H.; Asakura, K.; Iwasawa, Y. Characterization and selective oxidation catalysis of modified Pt particles on SbOx. *Appl. Catal., A* **2000**, *191*, 131–140.
- (49) Goodman, E. D.; Latimer, A. A.; Yang, A.-C.; Wu, L.; Tahsini, N.; Abild-Pedersen, F.; Cargnello, M. Low-Temperature Methane Partial Oxidation to Syngas with Modular Nanocrystal Catalysts. *ACS Appl. Nano Mater.* **2018**, *1*, 5258–5267.

(50) Kondratenko, V. A.; Berger-Karin, C.; Kondratenko, E. V. Partial Oxidation of Methane to Syngas Over γ -Al₂O₃-Supported Rh Nanoparticles: Kinetic and Mechanistic Origins of Size Effect on Selectivity and Activity. *ACS Catal.* **2014**, *4*, 3136–3144.

(51) York, A. P. E.; Xiao, T.; Green, M. L. Brief Overview of the Partial Oxidation of Methane to Synthesis Gas. *Top. Catal.* **2003**, *22*, 345–358.

(52) Balkus, K. J.; Eissa, M.; Levado, R. Oxidation of alkanes catalyzed by zeolite-encapsulated perfluorinated ruthenium phthalocyanines. *J. Am. Chem. Soc.* **1995**, *117*, 10753–10754.

(53) Schunk, S. A.; Titlbach, S.; Rosowski, F.; Mueller, R.; Schulz, C.; Xie, J.; Schaefer, S.; Loeser, P.; Wittich, K.; Weber, M.; Glaum, R. *Mixed Oxide Compromising Oxygen, Phosphorous, Tungsten and at Least on Metal from the Groups 8 to 11 of the Periodic Table of the Elements*; WIPO.

(54) Karbstein, A.; Weber, M.; Lahr, D.; Daniels, J.; Assenmacher, W.; Mader, W.; Rosowski, F.; Schunk, S. A.; Glaum, R. Mixed-Metal Monophosphate Tungsten Bronzes Containing Rhodium and Iridium. *Eur. J. Inorg. Chem.* **2021**, *2021*, 1459–1469.

(55) Schulz, C.; Pohl, F.; Driess, M.; Glaum, R.; Rosowski, F.; Frank, B. Selective Oxidation of n-Butane over Vanadium Phosphate Based Catalysts: Reaction Network and Kinetic Analysis. *Ind. Eng. Chem. Res.* **2019**, *58*, 2492–2502.

(56) Foppa, L.; Sutton, C.; Ghiringhelli, L. M.; De, S.; Löser, P.; Schunk, S.; Schaefer, A.; Scheffler, M. Learning design rules for selective oxidation catalysts from high-throughput experimentation and artificial intelligence. *ACS Catal.* **2022**, *12*, 2223.

(57) Roy, S. C.; Glaum, R.; Abdullin, D.; Schiemann, O.; Quang Bac, N.; Lii, K.-H. Solid Solution Formation between Vanadium(V) and Tungsten(V) Oxide Phosphate. *Z. Anorg. Allg. Chem.* **2014**, *640*, 1876–1885.

(58) Schunk, S.; Sundermann, A.; Hibst, H. Structure oriented library design in gas phase oxidation catalysis. *Catal. Today* **2008**, *137*, 36–43.

(59) Schunk, S. A.; Sundermann, A.; Hibst, H. Retrospective hit-deconvolution of mixed metal oxides: spotting structure-property-relationships in gas phase oxidation catalysis through high throughput experimentation. *Comb. Chem. High Throughput Screen.* **2007**, *10*, 51–57.

Recommended by ACS

Hydrogen Interaction with Oxide Supports in the Presence and Absence of Platinum

Arik Beck, Jeroen A. van Bokhoven, *et al.*

OCTOBER 10, 2022
THE JOURNAL OF PHYSICAL CHEMISTRY C

READ 

Role of an Interface for Hydrogen Production Reaction over Size-Controlled Supported Metal Catalysts

Dongjae Shin, Jeong Woo Han, *et al.*

JUNE 22, 2022
ACS CATALYSIS

READ 

Kinetic Diagnostics and Synthetic Design of Platinum Group Metal-Free Electrocatalysts for the Oxygen Reduction Reaction Using Reactivity Maps and Site Utilization Descr...

Fang Luo, Peter Strasser, *et al.*

JULY 21, 2022
JOURNAL OF THE AMERICAN CHEMICAL SOCIETY

READ 

Understanding and Modifying the Scaling Relations for Ammonia Synthesis on Dilute Metal Alloys: From Single-Atom Alloys to Dimer Alloys

Yining Zhang, Jiannian Yao, *et al.*

JULY 15, 2022
ACS CATALYSIS

READ 

Get More Suggestions >